

# Design and fabrication of highly hydrophobic Mn nano-sculptured thin films and evaluation of surface properties on hydrophobicity

Somaye Hosseini<sup>1</sup> · Hadi Savaloni<sup>2</sup> · Mehran Gholipour-Shahraki<sup>3</sup>

Received: 16 January 2017 / Accepted: 14 February 2017 / Published online: 11 March 2017  
© The Author(s) 2017. This article is published with open access at Springerlink.com

**Abstract** The wettability of solid surfaces is important from the aspects of both science and technology. The Mn nano-sculptured thin films were designed and fabricated by oblique angle deposition of Mn on glass substrates at room temperature. The obtained structure was characterized by field emission scanning electron microscopy and atomic force microscopy. The wettability of thin films samples was investigated by water contact angle (WCA). The 4-pointed helical star-shaped structure exhibits hydrophobicity with static WCAs of more than 133° for a 10-mg distilled water droplet. This sample also shows the rose petal effect with the additional property of high adhesion. The Mn nano-sculptured thin films also act as a sticky surface which is confirmed by hysteresis of the contact angle obtained from advancing and receding contact angles measurements. Physicochemical property of liquid phase could effectively change the contact angle, and polar solvents in contact with hydrophobic solid surfaces do not necessarily show high contact angle value.

**Keywords** Sculptured thin films · Hydrophobicity · Surface free energy · Cassie–Baxter state · Wenzel state · Petal effect

✉ Hadi Savaloni  
savaloni@khayam.ut.ac.ir

<sup>1</sup> Plasma Physics Research Center, Science and Research Branch, Islamic Azad University, Tehran, Iran

<sup>2</sup> Department of Physics, University of Tehran, North-Kargar Street, Tehran, Iran

<sup>3</sup> Physics Department, Faculty of Science, Arak University, Arak 38156-8-8349, Iran

## Introduction

There is a growing interest in hydrophobic surfaces due to their extensive applications in science and technology [1–3]. Roughness and symmetry [4–7] are the most effective factors to influence the hydrophobicity. Measurement of contact angle is a common method to describe the wettability of solid surfaces and their hydrophobicity. Surfaces with contact angle between 90° and 150° and more than 150° are considered as hydrophobic and super hydrophobic, respectively [8]. Natural and most of the synthetic hydrophobic surfaces consist of micro- and nano-structures simultaneously, but nanoscale structure considered less attractive by scientific research [7, 9].

Glancing or oblique angle deposition cares about the new generation of physical techniques for preparation of thin films with predesign morphology and desirable roughness. The rotation of the substrate about two axes during the deposition procedure could prepare condition for production of three-dimensional structures with anisotropic columns in 1–100 nm scale [10]. The deposition angle, rate of substrate rotation and solid material are the effective factors which control morphology, roughness, symmetry and porosity of structures.

In this study, Mn nano-sculptured thin films with different morphologies and structural properties are designed and fabricated by oblique angle deposition technique. The effects of structural properties (i.e., deposition angle, morphology, number and diameter of arms, roughness and void fraction) on thin films hydrophobicity are investigated.

## Experimental details

Mn (99.99% purity) helical star-shaped nano-sculptured thin films with different sizes and morphologies were deposited on glass substrate (microscope slide; 3 × 2 cm;

Thermo Scientific Menzel–Glaser, Soda lime glass) by electron beam evaporation from a graphite crucible of 6 mm diameter at room temperature. An Edwards (EdwardsE19 A3) coating plant with a base pressure of  $2 \times 10^{-7}$  mbar and a deposition rate of  $1 \text{ \AA s}^{-1}$  was used. In order to produce a uniform deposition on the substrates, distance between the evaporation source and the substrate was fixed at 30 cm. In this distance, evaporation source behave like a point source and due to the large mean free path ( $\sim 103$  to  $104$  cm) vapor has straight trajectories [11]. Reproducibility of the deposition results was confirmed by repeating the deposition a few times. A quartz crystal monitor (Sigma Instruments, SQM-160, USA) positioned close to the substrate for controlling the deposition rate. The mechanical movement of the substrate holder [rotation about its surface normal ( $\varphi$ ), the facility for dividing each revolution into different sectors and the speed of revolution] was controlled by the stepper motor which controlled through interface to a computer in which the related software (in the LabVIEW format) is written and installed. All these are domestic made. Prior to deposition, all glass substrates were ultrasonically cleaned sequentially in heated acetone and ethanol. The surface roughness of the substrates was measured by a Talysurf profilometer and AFM, and the root-mean-square (rms) substrate roughness (Rq) obtained using these methods was 0.3 and 0.9 nm, respectively.

In oblique angle deposition, growth angle of columns which is with respect to the surface normal is “ $\beta$ ” when vapor incident angle is “ $\alpha$ .” Experimental data of FESEM are more agreeable with Tait rule (Eq. 1) when deposition angles are larger than  $60^\circ$  and tangent rule when deposition angles are smaller than  $60^\circ$  (Eq. 2) [12].

$$\beta = \alpha - \sin^{-1} \left( \frac{1 - \cos \alpha}{2} \right) \quad (1)$$

$$\tan(\beta) = \frac{1}{2} \tan(\alpha) \quad (2)$$

Five different Mn nano-sculptured thin films, namely vertical nano-rod, inclined nano-rod, 3-pointed helical star, 4-pointed helical star and 5-pointed helical star, were produced with different deposition angles. The most influential deposition conditions are as follows:

Vertical and inclined nano-rod thin films were produced by deposition at  $\alpha = 0^\circ$  and  $\alpha = 45^\circ$  with films thickness of 500 and 200 nm, respectively, where the substrate holder was fixed ( $\varphi = \text{constant}$ ).

The Mn helical stars nano-sculptured were deposited in the following stages:

Stage 1: substrate was fixed in an arbitrary position ( $\varphi = 0^\circ$ ), and 60 nm Mn film was deposited.

Stage 2: substrate was rotated by  $180^\circ$  ( $\varphi = 180^\circ$ ), and at this new position (opposite to Stage 1) 60 nm Mn film was deposited (first tip point of the star is made).

Stage 3: substrate was rotated by  $180^\circ$  to return to the position of Stage 1 and then rotated by  $120^\circ$ ,  $90^\circ$  and  $72^\circ$  for deposition of 3-pointed helical star, 4-pointed helical star and 5-pointed helical star, respectively, and 60 nm Mn film was deposited.

Stage 4: substrate was rotated by  $180^\circ$  ( $\varphi = 180^\circ$ ), and at this new position (opposite to Stage 3) 60 nm Mn film was deposited (second tip point of the star is made).

Stage 5: substrate was rotated by  $180^\circ$  to return to the position of Stage 3 and then rotated by  $120^\circ$ ,  $90^\circ$  and  $72^\circ$  for deposition of 3-pointed helical star, 4-pointed helical star and 5-pointed helical star, respectively, and 60 nm Mn film was deposited.

Stage 6: substrate was rotated by  $180^\circ$  ( $\varphi = 180^\circ$ ), and at this new position (opposite to Stage 5) 60 nm Mn film was deposited (third tip point of the star is made).

Note: the first pitch of 3-pointed helical star is completed and should continue from Stage 11.

Stage 7: substrate was rotated by  $180^\circ$  to return to the position of Stage 5 and then rotated by  $90^\circ$  and  $72^\circ$  for deposition of 4-pointed helical star and 5-pointed helical star, and 60 nm Mn film was deposited.

Stage 8: substrate was rotated by  $180^\circ$  ( $\varphi = 180^\circ$ ), and at this new position (opposite to Stage 7) 60 nm Mn film was deposited (forth tip point of the 4-pointed helical star and 5-pointed helical star is made).

Note: the first pitch of 4-pointed helical star is completed and should continue from Stage 11.

Stage 9: substrate was rotated by  $180^\circ$  to return to the position of Stage 7 and then rotated by  $72^\circ$ , and 60 nm Mn film was deposited.

Stage 10: substrate was rotated by  $180^\circ$  ( $\varphi = 180^\circ$ ), and at this new position (opposite to Stage 9) 60 nm Mn film was deposited (fifth tip point of the star for 5-pointed helical star is made).

Stage 11: substrate was rotated by  $180^\circ$  to return to the position of Stage 9 (for 3-pointed helical star this position is Stage 5 and for 4-pointed helical star this position is Stage 7) and then rotated by  $72^\circ$  (for 3-pointed helical star rotate by  $120^\circ$  and for 4-pointed helical star rotate by  $90^\circ$ ).

One pitch of the helical Mn star-like structure is completed, and the substrate holder is in the position of Stage 1; Stages 1–11 may be repeated for fabrication of second and third pitches of the helical structures.

The second pitch and the third pitch of the sculptured structures were fabricated by repeating the above stages while the lengths of arms were decreased to 30 and 15 nm, respectively. Therefore, the final structure should look like a pine tree.

The film thicknesses and column shapes and sizes were measured by field emission electron microscope (FESEM) (Hitachi S-4100 SEM, Japan). The FESEM samples were coated with a very thin layer of gold to prevent the charging effect. The surface physical morphology and roughness were obtained by means of AFM (Park scientific instruments model autoprobe) analysis with a Si tip of 10 nm in diameter and in non-contact mode.

The static and dynamic contact angles were measured by domestic made instrument with a 5-diopter lens and digital camera (model DCR-SR200E, Sony, Japan). A 10-mg distilled water droplet was placed smoothly on the solid surfaces of the samples, and the image of static contact angle is recorded by using ImageJ software code and the method of Low-Bond Axisymmetric Drop Shape Analysis (LB-ADSA) [13]. Dynamic and hysteresis contact angles were measured according to the method described by Abelman et al. [14]. The advancing and receding contact angles were measured by pumping in and out further of liquid in initial droplet. The contact angle hysteresis is attributed to the difference between advancing and receding contact angles.

### Theory: surface free energy

There are several intermolecular bonds in the bulk of a material compared with the molecules on the surface. Therefore, surface has more energy that is named surface free energy (SEF) or interfacial energy. Surface free energy is calculated by Young equation:

$$\gamma_{sv} = \gamma_{sl} + \gamma_{lv} \cos \theta_Y \tag{3}$$

where  $\theta_Y$  is the contact angle between the liquid and the solid surfaces,  $\gamma_{lv}$  and  $\gamma_{sl}$  are liquid surface and surface-solid tensions, respectively.  $\gamma_{sl}$  was calculated by acid–base method (Eq. 4) which is described by Van Oss and Good [15, 16].

$$\gamma_{sl}^{\text{tot}}(1 + \cos \theta) = 2\sqrt{\gamma_s^{\text{LW}}\gamma_l^{\text{LW}}} + 2\sqrt{\gamma_s^{\text{LW}}\gamma_l^{\text{+}}} + 2\sqrt{\gamma_s^{\text{LW}}\gamma_l^{\text{-}}} \tag{4}$$

where  $\gamma_l^{\text{tot}}$  is the total surface tension of the liquid drop,  $\gamma_s^{\text{LW}}$  is Lifshitz–Van der Waals,  $\gamma^+$  is electron acceptor and  $\gamma^-$  is electron donor components.  $\theta$  is the contact angle, and  $s$  and  $l$  define solid and liquid, respectively.  $\gamma_s^{\text{LW}}$ ,  $\gamma_s^-$  and  $\gamma_s^+$  were calculated by measuring the contact angle between three different liquids ( $\alpha$ -bromonaphthalene, water and formamide) with known surface tensions (Table 1), and then, the values of solid surface tensions were obtained by using Eqs. 5 and 6.

$$\gamma_s^{\text{AB}} = 2\sqrt{\gamma_s^+\gamma_s^-}, \tag{5}$$

**Table 1** Components of surface tension at room temperature ( $\text{mJ m}^{-2}$ ) [6]

Liquid	$\gamma^{\text{tot}}$	$\gamma^{\text{LW}}$	$\gamma^+$	$\gamma^-$
$\alpha$ -Bromonaphthalene (apolar)	44.4	44.4	0	0
Water (polar)	72.8	21.8	25.5	25.5
Formamide (polar)	58	39	2.28	39.6

$$\gamma_s^{\text{tot}} = \gamma_s^{\text{LW}} + \gamma_s^{\text{AB}}, \tag{6}$$

where  $\gamma_s^{\text{AB}}$  is the polar component of Lewis acid–base interaction.

Works of adhesion and spreading that are dependent on the contact angle of water droplet on solid surfaces and water total surface tension were determined by Eqs. 7 and 8, respectively [17]:

$$W_a = \gamma_l^{\text{tot}}(\cos \theta + 1), \tag{7}$$

$$W_s = \gamma_l^{\text{tot}}(\cos \theta - 1). \tag{8}$$

Water surface tension also was used to calculate Laplace pressure [18] (Eq. 9):

$$P_L = \frac{2\gamma_{lv}}{R}, \tag{9}$$

where  $R$  is the water droplet radius on solid surface which is defined as:

$$R = \left[ 3V/\pi(1 - \cos \theta)^2(2 + \cos \theta) \right]^{1/3}, \tag{10}$$

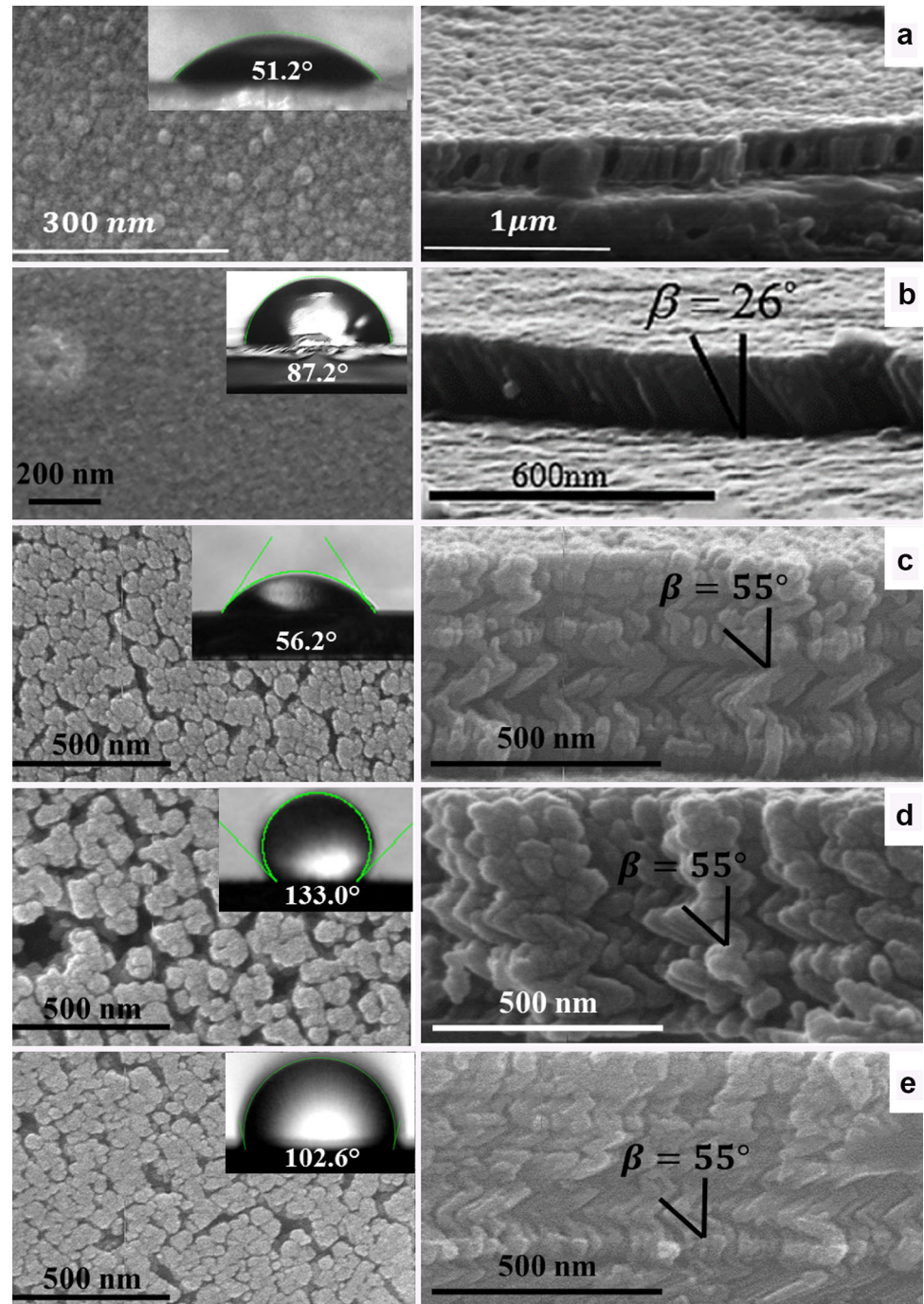
where  $V$  is droplet volume [19].

## Results and discussion

### FESEM and AFM analyses

The FESEM top and cross-sectional views of samples are shown in Fig. 1. Morphology of thin films indicates that Mn layers are deposited uniformly onto the substrate and their controlled growth, produced different shapes/nano-sculptured thin films. The thickness of pitches in each layer is less than 100 nm which were put together in specific configurations to make it possible to trap air bubble in pore body of structure and form rough surfaces. Structural characteristics of thin layer films are given in Table 2. As shown in Fig. 1, column width increases by increasing the films thickness and arm length and forms cone-shaped rough structure with cauliflower-like morphology. These results are in agreement with predation of structural zone model (SZM) which is suggested by Messier et al. [20]. In this model, evolutionary growth of structures is classified

**Fig. 1** FESEM images of surfaces and cross sections of nano-sculptured Mn thin films with different morphologies, vertical nano-rod (a); inclined nano-rod (b); 3-pointed helical star (c); 4-pointed helical star (d); 5-pointed helical star (e)



into different-size zones 1–3, 5–20, 20–40, 50–200 and 200–400 nm. The scaling of the column width will multiply 3 times per stage. The results of Messier's study showed that random ballistic aggregation of atoms leads to cluster structure in 1–3 nm scale.

During the development of nano-sculptured thin films, clustering and conical structure are formed. The low adatom mobility on Mn surfaces during low-temperature deposition causes cauliflower-like structure of about 10 nm

in size [20]. Savaloni et al. reported that increasing thin film thickness increases grain size and consequently the crystal structure and morphology change [21, 22].

Figure 2 shows AFM images of the two- and three-dimensional configuration of samples with different morphologies. Number of grain, grain sizes and surface roughness were calculated by applying Spip code and 2D image of each structure. The surface void fraction can be calculated as:

**Table 2** Structural characteristics of different Mn sculptured thin films designed for this work

Helical morphology	Deposition angle $\alpha$ (°)	Growth angle $\beta$ (°)	Number of arms	Arm thickness ( $t$ nm)	Number of pitches	Film thickness ( $T$ nm)	Arm length ( $L$ nm)	Mean diameter (nm)
Vertical nano-rod	0	0	1	15	0	500	500	12.8 ± 1.1
inclined nano-rod	45	26	1	18	0	180	200	16.2 ± 2.0
3-Pointed helical star	80	55.6	18	30	3	480	60 30 15	60.4 ± 2.3
4-Pointed helical star	80	55.6	24	60	3	500	60 30 15	68.1 ± 3.1
5-Pointed helical star	80	55.6	30	20	3	710	60 30 15	58.3 ± 1.6

$$\text{Void Fraction} = \left(1 - \frac{N \times A'}{A}\right) \times 100 \tag{11}$$

where  $N$ ,  $A'$  and  $A$  are number of grains, mean surface of top area of grains and total area of the 2D AFM image, respectively.

The surface void fraction is important specifics of nano-sculptured thin films which are produced by oblique angle deposition and self-shadowing effects. Figure 2a shows the AFM image of vertical nano-rod structure. As shown in Fig. 2a and first column of Table 3, in vertical deposition method void fraction is very low. For more investigation of surface properties, void fraction oblique angle deposition ( $\alpha = 45^\circ$ ) was used to fabricate inclined nano-rod structure (Fig. 2b). In this structure, column growth angle ( $\beta$ ) is  $26^\circ$  according to the tangent equation [12]. Self-shadowing effect increases void fraction of inclined nano-rod structure (Table 3), but there is not significant difference between void fraction of two nano-rod structures. In Fig. 2c–e, 3-, 4- and 5-pointed helical star-structured films deposited at  $80^\circ$  oblique angle are given. The difference in morphologies and size of grooves between all the samples is clearly observed. In these Mn sculptured thin films, lengths of arms in each pitch are the same, but number of arms is different. The growth (rise) angle of all of these structures is the same and equal to  $54.5^\circ$  according to the Tait equation [12]. The analyses of the AFM images indicate that the shadowing effect modifies void fraction of these structures.

**Solid surface wettability**

Contact angle is one of the common ways to measure the wettability of a surface. The contact angles between 10 mg

distilled water droplet and the thin film surfaces examined in this work are given in Table 3. The 4-pointed helical star structure thin film shows the highest static contact angle ( $133.1^\circ$ ), while contact angle of 5-pointed helical star, inclined nano-rod structure, 3-pointed helical star and the vertical nano-rod structure is  $102.6^\circ$ ,  $87.2^\circ$ ,  $56.2^\circ$  and  $52.2^\circ$ , respectively. Figure 1 shows the image of 10 mg distilled water droplet on the examined sample’s surfaces.

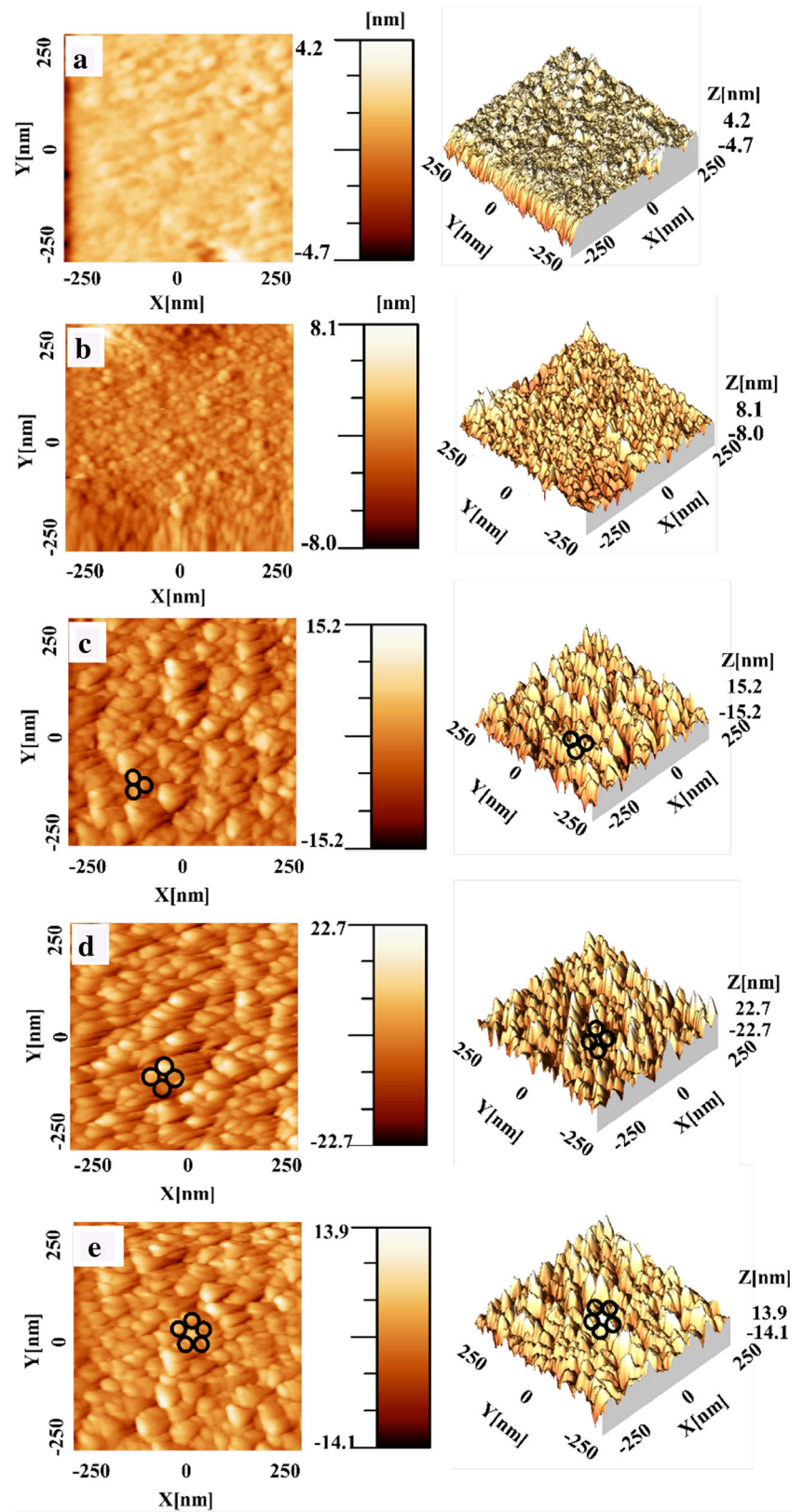
*Factors affecting the wettability of surfaces*

The contact angle and hydrophobic property of surface depend on their structural properties (roughness, void fraction, film thickness and symmetry) and almost certainly on the water droplet constituents.

*Influence of different structural parameters on the contact angle and the surface free energy*

As shown in Table 3 for all samples except 3-pointed helical star structure, slight increase in surface void fraction has led to increase in contact angle more than  $36^\circ$  (the void fraction of the samples (4- and 5-pointed helical stars, vertical and inclined nano-rod structure samples) changes as a result of self-shadowing effects of oblique angle deposition). The increase in deposition angle from  $45^\circ$  to  $80^\circ$  has led to a drastic increase in the 3- and 4-pointed helical star thin film void fraction, although the increase in the 5-pointed helical star is low when compared with other helical star samples. On the other hand, increase in void fraction is not always the cause of enhancement of surface hydrophobicity. Table 3 shows that the void fraction is higher in the 3-pointed helical star than in 5-pointed helical

**Fig. 2** 2D and 3D AFM images of nano-sculptured Mn thin films with different morphologies, vertical nano-rod (a); inclined nano-rod (b); 3-pointed helical star (c); 4-pointed helical star (d); 5-pointed helical star (e)



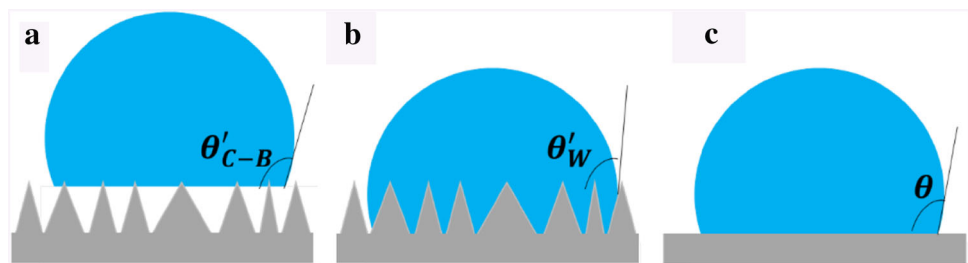
star and inclined nano-rod samples but contact angle is lower. Hence, there are some other structural parameters that may influence the surface hydrophobicity.

Comparison of the void fraction and surface roughness values in Table 3 for 3-pointed helical star and inclined nano-rod samples showed that these two major parameters

**Table 3** Structural characteristics of different Mn sculptured thin films designed for this work, work of adhesion ( $W_a$ ) ( $\text{mJ m}^{-2}$ ) and work of spreading ( $W_s$ ) ( $\text{mJ m}^{-2}$ ) for 3 different liquid drops on different types of sculptured structures produced in this work

Helical morphology	Void fraction (%)	$R_{\text{avg}}$ (nm)	$R_{\text{rms}}$ (nm)	Experimental static WCA ( $^\circ$ )	Cassie–Baxter predicted WCA	Wenzel predicted WCA	$R$ (mm)	Laplace pressure (Pa)	$W_a$	$W_s$
Vertical nano-rod	$12.2 \pm 0.2$	$1.4 \pm 0.8$	$1.8 \pm 0.2$	$51.2 \pm 0.4$	160.0	63.3	1.5	96.1	118.6	-27.1
Inclined nano-rod	$17.0 \pm 1.7$	$2.9 \pm 0.6$	$3.7 \pm 0.8$	$87.2 \pm 2.2$	163.7	63.2	2.6	55.9	76.5	-69.2
3-Pointed helical star	$40.9 \pm 3.4$	$5.7 \pm 0.3$	$7.0 \pm 0.3$	$56.2 \pm 1.8$	102.7	59.3	1.7	86.3	113.5	-32.3
4-Pointed helical star	$51.2 \pm 2.$	$8.6 \pm 0.8$	$10.6 \pm 0.7$	$133.0 \pm 1.4$	112.7	54.5	3.3	44.2	23.2	-122.4
5-Pointed helical star	$30.6 \pm 1.0$	$5.1 \pm 0.9$	$6.3 \pm 1.1$	$102.6 \pm 1.5$	116.9	59.3	2.9	49.6	57.0	-88.6

**Fig. 3** Surfaces wetting models. Rough surface and Cassie–Baxter model (a); rough surface and Wenzel model (b); flat surface (c)



are increased by  $\sim 23\%$  and 2.8 nm, respectively, but the contact angle of this sample is decreased by  $\sim 1.5$  degrees which may be due to arm length (the arm length is 60 and 200 nm for 3-pointed helical star and inclined nano-rod samples, respectively). Abdolsalam et al. [23] also showed that higher values of contact angles (higher hydrophobicity) may be achieved with longer nano-rods (nano-structure with longer arms).

Surface roughness is also another effective parameter on the hydrophobicity of surfaces. Increasing the surface roughness considerably increases the hydrophobicity of all samples except 3-pointed helical star structure (in all samples the contact angle increases about  $30^\circ$  by 3 nm increase in the surface roughness), but high surface roughness and void fraction of 3-pointed helical star do not enhance their hydrophobicity properties. 3-pointed helical star in compare with other helical star structures has more asymmetric structure. With regard to these results, it could be concluded that structural symmetry effectively enhances the hydrophobicity of solid surfaces.

Design and deposition of different Mn nano-sculptured thin films indicated that structural symmetry, surface

roughness and surface void fraction as result of shadowing effect ( $80^\circ$  deposition angle) may enhance hydrophobicity. Hence, from the obtained results, one may deduce that the higher contact angle ( $133^\circ$ ) obtained for the 4-pointed helical star nano-sculptured sample could be due to higher degree of symmetry, higher surface roughness (8.6 nm) and higher void fraction (51.28%) (Fig. 1; Fig. 2). Structural symmetry with roughness and void fraction of 5-pointed star sample led to lower contact angle ( $102.6^\circ$ ) than of 4-pointed star. Asymmetric structure in 3-pointed star leads to lowest contact angle between helical star structure ( $56.2^\circ$ ) and dominates influence of the void fraction and surface roughness.

*Rough surfaces wetting models*

Two main approaches are proposed in the literature to explain wetting property of rough surfaces, namely Cassie–Baxter state [24] and Wenzel state [25].

According to the Cassie–Baxter model, air is trapped between surface grooves and liquid droplet sits on top of the arms (Fig. 3a) and so the hydrophobicity increases. In this case, the relationship between the contact angle on the

**Table 4** Contact angles for 10 mg water droplet and surface free energy ( $\text{mJ m}^{-2}$ ) obtained from contact angle of 3 different liquid drops on different types of sculptured structures produced in this work

Helical morphology	Advancing WCA ( $^{\circ}$ )	receding WCA ( $^{\circ}$ )	Hysteresis WCA ( $^{\circ}$ )	$\theta$ ( $\alpha$ -bromonaphthalene) ( $^{\circ}$ )	$\theta_{\text{water}}$ ( $^{\circ}$ )	$\theta_{\text{formamid}}$ ( $^{\circ}$ )	$\gamma_s^{\text{LW}}$	$\gamma_s^+$	$\gamma_s^-$	$\gamma_{\text{AB}}$	$\gamma_s^{\text{tot}}$
Vertical nano-rod	$54.4 \pm 1.9$	$18.5 \pm 2.3$	35.9	$23.4 \pm 2.4$	$51.2 \pm 0.4$	$12.2 \pm 2.4$	40.8	3.3	16.1	14.6	55.4
Inclined nano-rod	$93.1 \pm 1.7$	$22.1 \pm 0.8$	71	$5.2 \pm 1.6$	$87.2 \pm 2.2$	$11.4 \pm 1.7$	44.2	8.3	2.1	8.4	52.6
3-Pointed helical star	$60.3 \pm 2.0$	$20.6 \pm 1.5$	39.7	$8.3 \pm 1.0$	$56.2 \pm 1.8$	$12.9 \pm 2.0$	43.9	3.2	7.0	16.7	60.7
4-Pointed helical star	$141.1 \pm 2.6$	$39.2 \pm 0.6$	101.9	$27.2 \pm 1.0$	$133.0 \pm 1.4$	$21.6 \pm 1.5$	39.6	21.0	65.9	74.4	114.0
5-Pointed helical star	$109.7 \pm 1.2$	$24.4 \pm 1.3$	85.3	$5.2 \pm 1.1$	$102.6 \pm 1.5$	$27.4 \pm 1.4$	44.2	8.5	11.8	20.0	64.3

smooth surface  $\theta$  and the contact angle on the rough surface  $\theta'$  is given as [24]:

$$\cos \theta' = \varphi - 1 + \varphi \cos \theta \quad (12)$$

where  $\varphi$  is an area fraction of liquid–solid interface and  $(1 - \varphi)$  is that of the solid–air interface, while  $\varphi$  can be considered as:

$$\varphi = \frac{N' \times A'}{S} \quad (13)$$

where  $N'$  is:

$$N' = \frac{N \times S}{A}, \quad (14)$$

and  $S$  can be obtained by defining the radius of the spherical drop as  $R$  and the radius of circular interface of liquid–solid as  $X$ , hence we have:

$$X = R \sin \theta, \quad (15)$$

and

$$S = \pi X^2. \quad (16)$$

According to Wenzel model, the penetration of water droplet between grooves of the structure decreases surface hydrophobicity and also its contact angle (Fig. 3b). In this case, the relationship between the contact angle formed on a smooth surface  $\theta$  and the contact angle formed on the rough surface  $\theta'$  is given as [25]:

$$\cos \theta' = R_1 \cos \theta, \quad (17)$$

where  $R_1$  is the ratio of the actual contact area of liquid–solid to the projected area.

Considering that the structures do not have an ordered geometrical shape, the following equation was used to obtain values of  $R_1$ :

$$R_1 = 1 + \frac{N' \times 2\pi r \times R_{\text{rms}}}{S}. \quad (18)$$

In this equation,  $r$  is the average grain radius and  $R_{\text{rms}}$  is the root-mean-square surface roughness.

Predicted contact angle values for samples obtained from Cassie–Baxter and Wenzel equations (Eqs. 12 and 17, respectively) are given in Table 3. By comparing experimental and theoretical data, it can be deduced that the vertical nano-rod, inclined nano-rod and 3-pointed helical star are in the Wenzel state and vertical 4-pointed helical star and 5-pointed helical star are in the Cassie–Baxter state.

It is worthy to note that there is slight difference between predicted and experimental contact angles which may depend on some anisotropy of sculptured thin films that is not considered in Eqs. 12 and 17.

The result of Laplace pressure in different samples is in agreement with hydrophobicity data (i.e., 4-pointed helical star structure with lowest Laplace pressure shows the largest contact angle). Increasing the Laplace pressure induced transition from Cassie–Baxter to Wenzel state.

### Rose petal effect

Surface free energy values for different samples examined in this work were calculated using acid–base method (Eqs. 4–6) by considering the contact angle for three different liquids ( $\alpha$ -bromonaphthalene, formamide and distilled water) which are given in Table 4. Except 3-pointed helical star structure, all surface free energies of samples in this work are increased with surface roughness (i.e., 4-pointed helical star structure shows highest surface free energy). Results are in agreement with theoretical study on role of surface roughness on the surface free energy [26]:



$$\gamma_s^{\text{tot}} = W = \frac{1}{N} \sum_i^N \vec{F}_i \cdot \vec{r}_i = \frac{1}{N} F_c \cdot \sum_i^N \vec{r}_i \sim F_c R_{\text{rms}}, \tag{19}$$

where  $F_c$  is the constant adhesion force,  $R_{\text{rms}}$  is the root-mean-square surface roughness,  $W$  is the average work done by the adhesion force vector on the surface as the tip of the AFM moves the displacement vector  $\vec{r}_i$ .  $\vec{F}_i$  is the adhesion force which can be obtained from the spring constant of the AFM tip.  $N$  is the number of samples. According to this equation, the surface energy increases with increasing surface roughness.

The application of hydrophobic surfaces depends on droplet behavior on the surfaces and their wettability. Natural superhydrophobic surfaces classified into two groups: slippery and sticky [27, 28]. Both of these superhydrophobic surfaces exhibit a large contact angle, but water droplet shows weak and strong adhesion onto slippery and sticky superhydrophobic surfaces, respectively, according to their contact angle hysteresis [27, 28]. In sticky case, the water droplet is strongly pinned on the surface, even when the surface is upside down which is called rose petal effect [28], while in case of slippery surfaces water droplet can easily move on the surface and make self-cleaning property which is so called lotuses effect.

As shown in Table 3, 4-pointed helical star structure has highest work of adhesion and work of spreading values that means this surface is hydrophobic. Surfaces, with contact angle hysteresis (difference between advancing and receding contact angle) higher than 20°, can show large adhesion property [29]. It can be seen that all of the contact angle hysteresis values are higher than 20° with the highest value obtained for 4-pointed helical star structure. Hence, it can be considered that these samples are sticky surfaces. The result of contact angle hysteresis (Table 4) showed that this property is related to the structural property and their hydrophobicity. By increasing samples hydrophobicity, contact angle hysteresis and adhesion increase. Therefore, 4-pointed helical star hydrophobic structure with contact angle of 133° and contact angle hysteresis of 101.9° is a hydrophobic sticky surface which is acting as a rose petal surface.

### The effects of physicochemical property of liquid phase on contact angle

#### The effect of liquid polarization

Not only substrate structural property influences contact angle between liquid and solid surfaces but also

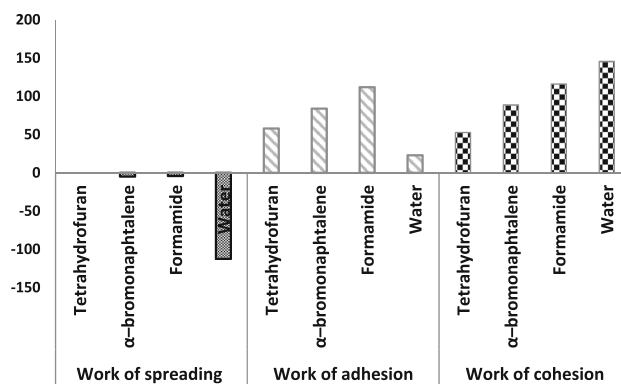


Fig. 4 Work of spreading, adhesion and cohesion of different solvent onto the 4-pointed helical star structure

physicochemical property of liquid phase could effectively change the contact angle.

In order to investigate the chemical property, solvents with different polarizations were selected and their contact angle onto the 4-pointed helical star structure was studied. As illustrated in Fig. 4, water has the highest work of cohesion and spreading when compared with other solvents. Therefore, in contact with hydrophobic surface, it shows largest contact angle. The different behaviors of formamide, tetrahydrofuran, water and  $\alpha$ -bromonaphthalene at solid liquid interface may be due to their polarization, viscosity and surface tension. Formamide has highest dipole momentum (3.4 D) while dipole momentum of tetrahydrofuran, water and  $\alpha$ -bromonaphthalene are 1.7, 1.8 and 0.0 D, respectively [30]. Viscosity is one of the main factors in formation of droplet which are 3.30, 0.48 and 0.89 mPa s for formamide, tetrahydrofuran and water, respectively, whereas viscosity of  $\alpha$ -bromonaphthalene is negligible [30]. Surface tension of formamide, tetrahydrofuran, water and  $\alpha$ -bromonaphthalene at 20 °C is 58.20, 26.40, 72.8 and 44.4 mN/m [31], respectively. These parameters are responsible for contact angle variation of liquid droplet on solid surfaces, but quantifying the impact of parameters subjects to some complications and needs some further investigations. Hence, polar solvents in contact with hydrophobic solid surfaces do not necessarily show high contact angle value.

#### The effect of total dissolved solids (TDS) on contact angle

Concentration of calcium carbonate in water could be an important parameter in contact angle measurements. This was studied by using four different dissolved solid concentrations in 10 mg water droplet. The results of contact angle onto the 4-pointed helical star structure, resistivity and TDS concentrations are shown in Fig. 5. It can be seen that the contact angle (hydrophobicity) increases with TDS

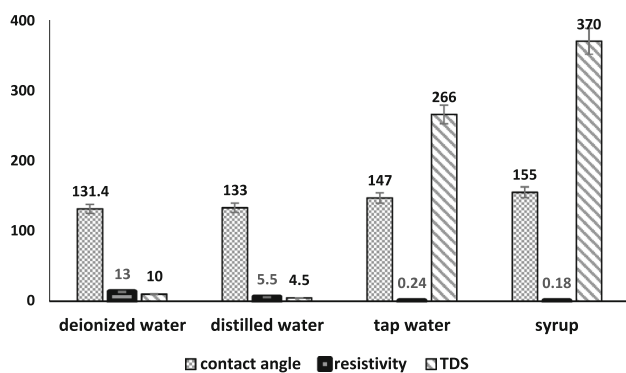


**Fig. 5** Contact angle of 10 mg water with different TDS concentration onto the 4-pointed helical star structure (electrical conductivity is directly related to TDS). Sucrose syrup (370  $\mu\text{g/l}$ )

which has led to increased viscosity and surface free energy. The aforementioned discussion indicates that an increase in viscosity and surface free energy could enhance hydrophobicity as a result of increased  $W_a$ ,  $W_c$  and  $W_s$ . It can be seen that the distilled water has lowest TDS concentration in 10 mg droplet. Hence, in order to achieve more accurate contact angle values, distilled water is a good choice.

## Conclusion

In this study, hydrophobic nano-sculptured thin films with different roughness were fabricated and the result showed that structures which trap air pocket between grooves are more hydrophobic. By increasing roughness, void fraction and structural symmetry contact angle (hydrophobicity) increased. In addition, the wetting model of 4- and 5-pointed helical star structures was described by Cassie–Baxter equation, while other structures, namely vertical nano-rod, inclined nano-rod and 3-pointed helical star, were in Wenzel state. All of the Mn nano-sculptured thin films indicate contact angle hysteresis higher than  $20^\circ$  that means these surfaces are acting as a sticky superhydrophobic surface with petal effect. The physicochemical property of the surface with 4-pointed star-like helical structure was examined for different liquids with different polarities (i.e., formamide, tetrahydrofuran, water and  $\alpha$ -bromonaphthalene), and it was found that water has the highest work of cohesion and spreading as well as largest contact angle. As this issue is affected by many parameters, further investigations are needed to make a more elaborate conclusion.

**Acknowledgements** This work was carried out with the support of the University of Tehran. HS gratefully acknowledges the Iran National Science Foundation (INSF) and the Centre of Excellence for Physics of Structure and Microscopic Properties of Matter,

Department of Physics, University of Tehran, for partial support of this work.

**Open Access** This article is distributed under the terms of the Creative Commons Attribution 4.0 International License (<http://creativecommons.org/licenses/by/4.0/>), which permits unrestricted use, distribution, and reproduction in any medium, provided you give appropriate credit to the original author(s) and the source, provide a link to the Creative Commons license, and indicate if changes were made.

## References

- Lafuma, A., Quere, D.: Superhydrophobic states. *Nat. Mater.* **2**, 457–460 (2003)
- Bingwei, X., Jingcheng, H.: Reversibly switchable wettability. *Chem. Soc. Rev.* **39**, 769–782 (2010)
- Yang, C., Tartaglino, U., Persson, B.N.J.: Influence of surface roughness on superhydrophobicity. *Phys. Rev. Lett.* **97**, 1161–1163 (2006)
- Ichimura, K., Oh, S.K., Nakagawa, M.: Light-driven motion of liquids on a photoresponsive surface. *Science* **288**, 1624–1629 (2000)
- Gleiche, M., Chi, L.F., Fuchs, H.: Nanoscopic channel lattices with controlled anisotropic wetting. *Nature* **403**, 173 (2000)
- Guo, Z.G., Fang, J., Hao, J.C., Liang, Y.M., Liu, W.M.: A Novel approach to stable superhydrophobic surfaces. *Chem. Phys. Chem.* **7**, 1674 (2006)
- Shang, H.M., Wang, Y., Limmer, S.J., Chou, T.P., Takahashi, K., Cao, G.Z.: Optically transparent superhydrophobic silica-based films. *Thin Solid Films* **472**, 37–43 (2005)
- Zhang, X., Shi, F., Niu, J., Jiang, Y., Wang, Z.: Superhydrophobic surfaces: from structural control to functional application. *J. Mater. Chem.* **18**, 621–633 (2008)
- Ebert, D., Bhushan, B.: Durable lotus-effect surfaces with hierarchical structure using micro and nanosized hydrophobic silica particles. *J. Colloid Interface Sci.* **368**, 584–591 (2012)
- Siabi-Garjan, A., Savaloni, H.: Extinction spectra and electric near-field distribution of Mn nano-rod based sculptured thin films: experimental and discrete dipole approximation results. *Plasmonics* **10**, 1007–1011 (2014)
- Eckertova, L.: *Physics of Thin Films*, 2nd edn, pp. 28–49. Plenum Press, Berlin, Springer (1986)
- Messeier, R., Giri, A.P., Rou, R.A.: Revised structure zone model for thin film physical structure. *J. Vac. Sci. Technol. A* **2**, 496–500 (1984)
- Stalder, A.F., Kulik, G., Sage, D., Barbieri, L., Hoffmann, P.: A snake based approach to accurate determination of both contact points and contact angles. *Colloids Surf. A* **286**, 92–103 (2006)
- Abelman, L., Lodder, C.: oblique evaporation and surface diffusion. *Thin Solid Films* **305**, 1–5 (1997)
- van Oss, C.J., Good, R.J., Chaudhury, M.K.: The role of van der Waals forces and hydrogen bonds in “hydrophobic interactions” between biopolymers and low energy surfaces. *J. Colloid Sci.* **111**, 378–390 (1986)
- van Oss, C.J.: *Interfacial Force in Aqueous Media*, pp. 9–48. Taylor & Francis, New York (2006)
- Israelachvili, J.N.: *Intermolecular and Surface Forces*, 2nd edn, pp. 223–281. Academic Press, London (1985)
- Butt, H.J., Graf, K., Kappl, M.: *Physics and Chemistry of Interfaces*, 2nd edn, ScienceDirect, pp. 8–9. Wiley-VCH Verlag, Weinheim (2003)
- Extrand, C.W.: A thermodynamic model for wetting free energies from contact angles. *Langmuir* **19**, 646–649 (2002)



20. Messeier, R., Giri, A.P., Rou, R.A.: Revised structure zone model for thin film physical structure. *J. Vac. Sci. Tech. A* **2**, 496–500 (1984)
21. Savaloni, H., Player, M.A.: Influence of deposition conditions and of substrate on the structure of uhv deposited erbium films. *Vacuum* **46**, 167–172 (1995)
22. Savaloni, H., Player, M.A.: Morphological changes in UHV deposited Er/a-C films: nucleation, growth and grain structure. *Thin Solid Films* **256**, 48–54 (1995)
23. Abdelsalam, M.E., Bartlett, P.N., Kelf, T., Baumberg, J.: Wetting of regularly structured gold surfaces. *Langmuir* **21**, 1753–1757 (2005)
24. Baxter, S., Cassie, A.B.D.: The water repellency of fabrics and a new water repellency test. *J. Text.* **36**, 67–90 (1946)
25. Wenzel, R.N.: The evaluation of textile waterproofing agents. *Surf. Coat. Technol.* **25**, 505–514 (1936)
26. Sun, C.C., Lee, S.C., Hwang, W.C., Hwang, J.S., Tang, I.T., Fu, Y.S.: Surface free energy effects in sputter-deposited W<sub>N</sub>x films. *Metall. Trans. A* **47**, 2533–2539 (2006)
27. Stark, A.Y., Badgeb, I., Wucinicha, N.A., Sullivana, T.W., Niewiarowska, P.H., Dhinojwala, A.: Surface wettability plays a significant role in gecko adhesion underwater. *PNAS* **16**, 6340–6346 (2013)
28. Barthlott, W., Neinhuis, C.: Purity of the sacred lotus, or escape from contamination in biological surfaces. *Planta* **202**, 1–8 (1997)
29. Stanton, M.M., Ducker, R.E., MacDonald, J.C., Lambert, C.R., McGimpsey, W.G.: Super-hydrophobic, highly adhesive, polydimethylsiloxane (PDMS) surfaces. *J. Colloid Interface Sci.* **367**, 502–508 (2012)
30. Smith, J.W.: Some developments of Guggenheim's simplified procedure for computing electric dipole moments. *Trans. Faraday Soc.* **46**, 394–399 (1950)
31. Wypych, G.: *Handbook of Solvents*, pp. 1453–1454. ChemTec Publishing, Victoria (2001)

